CLINICAL ORAL IMPLANTS RESEARCH

Vincent M. J. I. Cuijpers
Jacub Jaroszewicz
Sukumaran Anil
Abdullah Al Farraj Aldosari
X. Frank Walboomers
John A. Jansen

Resolution, sensitivity, and *in vivo* application of high-resolution computed tomography for titanium-coated polymethyl methacrylate (PMMA) dental implants

Authors' affiliations:
Vincent M. J. I. Cuijpers, X. Frank Walboomers, John A. Jansen, Department of Biomaterials, Radboud University Nijmegen Medical Centre, P.O. Box 9101 6500 HB, Nijmegen, The Netherlands
Jacub Jaroszewicz, Faculty of Materials Science and Engineering, Warsaw University of Technology, Wołoska 141, Warszawa 02-507, Poland
Sukumaran Anil, Department of Periodontics and Community Dentistry, College of Dentistry, King Saud University, Riyadh, Saudi Arabia
Abdullah Al Farraj Aldosari, Department of Prosthetic Dental Science, College of Dentistry, King Saud University, Riyadh, Saudi Arabia

Corresponding author:
Prof. DR. J. A. Jansen
Department of Biomaterials, Radboud University Nijmegen Medical Centre
P.O. Box 9101 6500 HB, Nijmegen
The Netherlands
Tel.: +3124-3614920
Fax: +3124-3614657
e-mail: j.jansen@dent.umcn.nl

Date:
Accepted 22 December 2012

To cite this article:
Cuijpers VMJI, Jaroszewicz J, Anil S, Al Farraj Aldosari A, Walboomers XF, Jansen JA. Resolution, sensitivity, and *in vivo* application of high-resolution computed tomography for titanium-coated polymethyl methacrylate (PMMA) dental implants.
Clin. Oral Impl. Res. **00**, 2013, 000–000
doi: 10.1111/clr.12128

Key words: bone–implant contact, micro-computed tomography, titanium-coated PMMA implants

Abstract

Objectives: The aims of this study were (i) to determine the spatial resolution and sensitivity of micro- versus nano-computed tomography (CT) techniques and (ii) to validate micro- versus nano-CT in a dog dental implant model, comparative to histological analysis.

Material and methods: To determine spatial resolution and sensitivity, standardized reference samples containing standardized nano- and microspheres were prepared in polymer and ceramic matrices. Thereafter, 10 titanium-coated polymer dental implants (3.2 mm in Ø by 4 mm in length) were placed in the mandible of Beagle dogs. Both micro- and nano-CT, as well as histological analyses, were performed.

Results: The reference samples confirmed the high resolution of the nano-CT system, which was capable of revealing sub-micron structures embedded in radiodense matrices. The dog implantation study and subsequent statistical analysis showed equal values for bone area and bone–implant contact measurements between micro-CT and histology. However, because of the limited sample size and field of view, nano-CT was not rendering reliable data representative of the entire bone–implant specimen.

Conclusions: Micro-CT analysis is an efficient tool to quantitate bone healing parameters at the bone–implant interface, especially when using titanium-coated PMMA implants. Nano-CT is not suitable for such quantification, but reveals complementary morphological information rivaling histology, yet with the advantage of a 3D visualization.

In current dentistry, titanium implants are often used. The success rate of an implant is characterized by the presence of direct contact between the implant surface and surrounding bone. The bright field microscopy of histologically stained slices remains the most frequently used tool for qualitative and quantitative evaluation of the bone response to an implant material in preclinical studies. Other conventional methods such as transmission electron microscopy (TEM), scanning electron microscopy (SEM), and atomic force microscopy (AFM) are available to study the bone–implant interface. Likewise, such two-dimensional analysis techniques are not completely representative of the whole specimen. As a result, also computed tomography (CT) is used frequently as a non-invasive non-destructive three-dimensional (3D) method to study radiopaque structures. On a microscopical level, the micro-CT technique is useful to determine bone volume and bone structural parameters (Stoppie et al. 2005; Chappard et al. 2008; Bonnet et al. 2009).

Still, the micro-CT technique for research approaches in bone has three major shortcomings. First, micro-CT systems contain various limitations, which restrain the image reconstruction and final quantification (Shalabi et al. 2007; Cha et al. 2009; Stock 2009). Reconstruction artifacts, reconstruction center errors, mechanical imperfections (such as specimen axis wobble and rotation axis misalignment), and beam hardening can occur. Some of the limitations can be corrected using software algorithms, for example, for beam hardening and ring reduction (Stoppie et al. 2007; Banhart 2008; Zou et al. 2011). The occurrence of scattering at the titanium implant–bone interface is a second problem.

For research purposes, scattering can be greatly reduced when polymer implant materials are used, which are equipped with a titanium surface coating (Shalabi et al. 2007). The third limitation is the resolution of conventional micro-CT, which is inferior to conventional two-dimensional (2D) microscopic images. To overcome these problems, higher spatial resolution and contrast sensitivity are required. Possibly, this can be achieved using CT systems at sub-micron resolution, such as synchrotron-CT (SRμCT), SEM-based nano-CT instruments, and stand-alone tube-based nano-CT systems (Banhart 2008; Stock 2009). However, comparative studies of the 3D bone–implant interface area between the micro- and nano-CT approaches have not been performed yet.

In view of the above-mentioned facts, the goal of this study was dual. Firstly, it was aimed to determine the spatial resolution and sensitivity of micro- versus nano-CT using standardized samples composed of well-defined synthetic microspheres embedded in matrices of varying X-ray absorption coefficients. Secondly, the objective was to validate the micro- versus nano-CT technique *in vivo*. For this purpose, titanium-coated polymethyl methacrylate (PMMA) implants were placed in the mandible of Beagle dogs, a frequently used model for biomedical implant interface studies (Calvo Guirado et al. 2009; Junker et al. 2011). After harvesting and fixing the biological specimens, *ex vivo* micro-CT and nano-CT were performed and compared with descriptive histology and histomorphometry.

Materials and methods

Standardized nano- and microsphere samples

Standardized polymethylcrylate (PMA) poly (1-phenylethane-1,2-diyl), polystyrene (PS), silicon dioxide (SiO_2) (all from Fluka, Buchs, Switzerland), and titanium dioxide (TiO_2) (Corpuscular, Cold Spring, NY, USA) nano- and microspheres of different sizes were used to determine the spatial resolution of the used micro- and nano-CT systems. The selected spheres ranged in size from 500 nm to 100 μm. The nano- and microsphere density (g/cm^3) and solid content (%WT) data were used to create a uniform solution. The particle solution ranged from $3.5*10^4$ of the 100-μm spheres to $1.3*10^{12}$ of the 500-nm spheres, per milliliter (Table 1).

Subsequently, 100 μl of the sphere solution was centrifuged 5 min at $4.8*10^3$ rpm. The supernatant was removed, and the spheres were dried overnight at 37°C. Thereafter, the spheres were mixed with, respectively, silicone rubber and calcium phosphate cement (CPC) matrices.

Table 1. **Composition, size, density, solid content, and particles per milliliter of micro- and nanospheres**

Particle composition	Particle size (μm/nm)	Density (g/cm3)	Solid content (% WT)	Particles//ml
Polystyrene	100 μm	1.05	2	$3.5*10^4$
	10 μm	1.05	2	$3.5*10^7$
	1 μm	1.05	2	$3.5*10^{10}$
Polymethacrylate	100 μm	1.19	10	$2.0*10^5$
	50 μm	1.19	10	$1.6*10^6$
	20 μm	1.19	10	$2.5*10^7$
SiO_2	1 μm	1.8–2	2,5	$7.9*10^{10}$
	500 nm	1.8–2	5	$1.3*10^{12}$
TiO_2	1 μm	2.2	2.2	$8.1*10^{10}$
	500 nm	2.2	2.5	$7.3*10^{11}$

Silicone rubber samples were created as follows. Each sphere type was mixed with a total volume of 0.7 ml of silicone compound (Elastosil RT 601 B and Elastosil RT 601 A, ratio 1:20; Wacker Silicones, Riemerling, Germany) and placed in an Eppendorf tube (Eppendorf AG, Hamburg, Germany). After overnight polymerization at 37°C, the silicone samples were removed from the tubes.

CPC consisting of 0.5 g calcium phosphate mixture (85% α-tri-calcium phosphate (Cam Bioceramics B.V., Leiden, The Netherlands), 10% $CaHPO_4$ (Sigma, St. Louis, MO, USA), and 5% $HCa_5O_{13}P_3$ (J.T. Baker Chemical Co, Phillipsburg, NJ, USA) was blended for 20 s with each type of sphere. Thereafter, 190 μl of 2% Na_2HPO4 (Merck, Darmstadt, Germany) solution was added and thoroughly mixed for 20 s. The thus-obtained deformable paste was placed in cylindrical Teflon molds, and the CPC was hardened overnight at 37°C.

Both silicone rubber and CPC samples were finally trimmed to a fixed volume of approximately 8 mm^3 for further micro- and nano-CT analysis.

To confirm sphere size, surface texture, and distribution of the nano- and microspheres in both samples, SEM analysis was performed. The specimens were coated using a 30-nm thin layer of Au–Pd, using a high-resolution sputter coater (208HR; Cressington Scientific, Watford, UK), and imaged using a field emission SEM (JSM 6330F; JEOL Corporation, Tokyo, Japan) operated at an accelerating voltage of 3 keV.

Implant design

Custom-made PMMA implants (3.2 mm in Ø by 4 mm in length) were used. All implants were coated with titanium (Ti), using a radio frequency magnetron sputtering unit (Edwards ESM 100, Crawford, UK). During the sputtering process, a commercially pure Ti target was used. The Ti target was sputter-cleaned before deposition. The target was considered clean when the plasma turned from pink to blue, resulting from blue light–emitting Ti in the plasma. Pressure was kept at 5.0×10^{-3} mbar using argon gas (4 l/h), and the power was set at 100 W. Thereafter, the PMMA implants were sputter-coated for 3 × 5 min, with a rotation of the implant of 120° before each time step to ensure homogenous coverage. The coating thickness was determined to be 10 nm using a Nanoscope IIIA atomic force microscope (Veeco Industries, Santa Barbara, CA, USA). Before use in the animal study, the implants were autoclaved for 15 min at 121°C.

Implantation procedure and implant retrieval

Ten adult Beagle dogs (1–2 years old, weight 10–12 kg) were used. The research protocol was approved by the ethical committee of King Saud University (Riyadh, Kingdom of Saudi Arabia), and national guidelines for care and use of laboratory animals were observed. The animals were anesthetized, and after intubation, general anesthesia was maintained with Isoflurane® (Rhodia Organique Fine Limited, Avonmouth, Bristol, UK).

In a first surgical session, three premolars (P2-4) were delicately removed in the left side of the mandible. Healing time for the extraction sockets was 3 months.

In a second surgical session, in the left side of the mandible of the 10 Beagle dogs, 10 implants were placed, that is, one implant per dog. To reduce peri-operative bleeding, local anesthesia was performed with 2% lidocaine-containing epinephrine (1 : 100,000). Before surgery, the local mucosa was cleaned with a 10% povidone-iodine and incised. A bone defect of 3.2 mm in diameter by 8 mm in depth was created by drilling, using low rotational drill speeds (800–1200 rpm) and continuous external cooling with saline. The implant was placed press-fit at the bottom of

the defect. Finally, the gingiva was sutured and all implants were left in a submerged position for an implantation time of 4 weeks. After surgery, Finadyne® (Schering corporation, Kenilworth, NJ, USA) and a broad-spectrum antibiotic (Gentamycin, SPIMACO, Qassim, Saudi Arabia, 4 mg/kg body weight intramuscularly) were given for 7 days.

At the end of the implantation period, the animals were euthanized by an overdose of pentobarbital, and the implants with surrounding tissue were harvested. The specimens were fixed in 10% neutral-buffered formalin solution with subsequent dehydration in a graded series of ethanol (70–100%). Thereafter, specimens were hemi-sectioned. The top part was used for micro-CT and subsequent nano-CT analysis. For nano-CT, it was necessary to reduce the size of the specimen further, as the maximum size for nano-CT specimens was approximately 2.5 × 2.5 × 2.5 mm. Sectioning and reduction of the specimen were performed using a Leica EM TXP target preparation device (Leica Microsystems, Wetzlar, Germany), with a 300-μm diamond-coated disk cutter blade. The bottom part was used to prepare histological sections.

Micro- and nano-computed tomography

The standardized samples, as well as the implant samples, were scanned using the Skyscan Micro-CT system model 1172 and nano-CT system model 2011 V 2.3 (Skyscan, Kontich, Belgium). Selection of these systems was based on the minimal image pixel size, 0.8 μm and 150 nm, respectively (Sasov et al. 2008).

The SkyScan 1172 system was operated at 100 kV and 100 μA, and the exposure time was set to 260 ms. Scanning was performed by 180° rotation around the vertical axis and with a rotation step of 0.5°. During scanning, 0.5-mm aluminum filter was used. The necessary field of view (FOV) for the standardized and implant samples was determined, resulting in an optimal image pixel size of 3 and 4.37 μm, respectively. Subsequently, the projected images were reconstructed in 2000 × 2000 pixel-sized cross-sectional images using the Skyscan NRecon® cone beam reconstruction software with beam-hardening compensation and ring artifact correction set to 30% and 15, respectively.

For nano-CT, samples were scanned 180° around the vertical axis in rotation steps of 0.3 degrees. The X-ray source was set to a voltage of 40 kV and current of 180 μA. The exposure time was 2.0 s using a detector of 1280 × 1280 pixels. Raw data were reconstructed with the NRecon® cone beam reconstruction software. Images with pixel size of 500 nm and 2 μm were generated from the standardized and implant samples, respectively. As a result, the FOV was 2.56 × 2.56 mm; that is, capable of including the entire specimen.

Micro- and nano-computed tomography analysis

Skyscan CTAn V.1.11 software was used for segmentation, registration, and quantification of all reconstructed images. The obtained images of the standardized samples were used to determine resolution and sensitivity limit. The digital ruler of the CTAn software program was used to measure the smallest visible sphere present in 10 representative images, with known image pixel size. The variation in radiodensity was detected using the gray scale histogram (range 0–255) values of the complete data set of the standardized sample.

For the implant samples, bone regeneration, routinely, is detected in a 500-μm zone from the surface of the implant (Schouten et al. 2009; Junker et al. 2010a,b). Thus, in 2D cross sections of the reconstructed CT images, a standardized threshold of the gray values for bone within the total data was set. Then, the bone area (BA) percentage was analyzed in the region of interest (ROI) zone of 500 μm surrounding the implant.

Further, for the complete 3D reconstructions, the bone volume (BV) percentage was calculated in a fixed volume of interest (VOI) zone of 500 μm surrounding the implant surface with a depth of 2 mm. Also, the bone-to-implant contact (BIC) percentage was calculated using an algorithm including automated adaptive segmentation of the bone and morphology-based operations as dilatation.

Histology and histomorphometry

The bottom part of the specimens was embedded in epoxy resin (EpoFix®; Struers, Rødovre, Denmark). After polymerization, thin sections of the implants were prepared using a modified SP1600 inner circular sawing microtome (Leica; van der Lubbe et al. 1988) and stained with methylene blue and basic fuchsin. The sections were made in a cross-sectional direction perpendicular to the longitudinal implant axis. Acquisition of microscopical images and histological evaluation were performed using an automated light microscope (Axio Imager Z1; Carl Zeiss Micro Imaging GmbH, Göttingen, Germany). With the aid of the digital image processing software module MosaiX of the Axiovision V4.6.3 software package combined with a motorized microscope stage, a high-resolution image (0.27 μm pixel size) of the complete ROI was obtained.

For the final image quantification, a computer-based image analysis system (Leica QWIN Pro image analysis software; Leica Imaging Systems, Cambridge, UK) was used. For calibrating the Leica QWIN quantification program for further histomorphometric analysis of the microscopic images, the known pixel size was imported.

The ROIs of corresponding planes of the 2D micro-CT and histological slices were quantified in μm^2. The BA percentage was determined in a 500-μm ROI zone from the implant surface, and the BIC percentage was calculated using the perimeter of the implant and total of contact parts of bone tissue with the implant surface.

Statistical analysis

The mean gray values of both silicone and CPC matrices when using micro- and nano-CT were compared using an unpaired t-test (InStat, version 3.05; GraphPad Software Inc., San Diego, CA, USA). Statistical analysis of BA, BV, and BIC percentage measurements of the different samples using both CT techniques and histology were conducted using paired t-tests (SPSS version 20, IBM Statistics, Armonk, NY, USA). For repeated testing of BA and BIC, Bonferroni correction was applied.

Results

Standardized samples

Using SEM, all four types of micro- and nanospheres were detected by visual inspection and observed to be distributed evenly in both silicone rubber and CPC matrices. The rough surface of CPC made it more difficult to distinguish 1-μm and 500-nm spheres in CPC (Fig. 1).

The micro-CT system allowed the detection of the 10- and 100-μm microspheres inside the silicone rubber as well as CPC matrix. On the other hand, due to limitations in spatial resolution, the one-micron spheres could only be detected using the nano-CT system, while the 500-nm spheres could not be detected at all.

The sensitivity limits were also determined. After normalization, the gray value ranges in the histograms of the radio absorption in micro-CT were 31–124 (mean 49.0 ± 19.3) for silicone matrices and 55–187 (mean 104.3 ± 21.7) for CPC

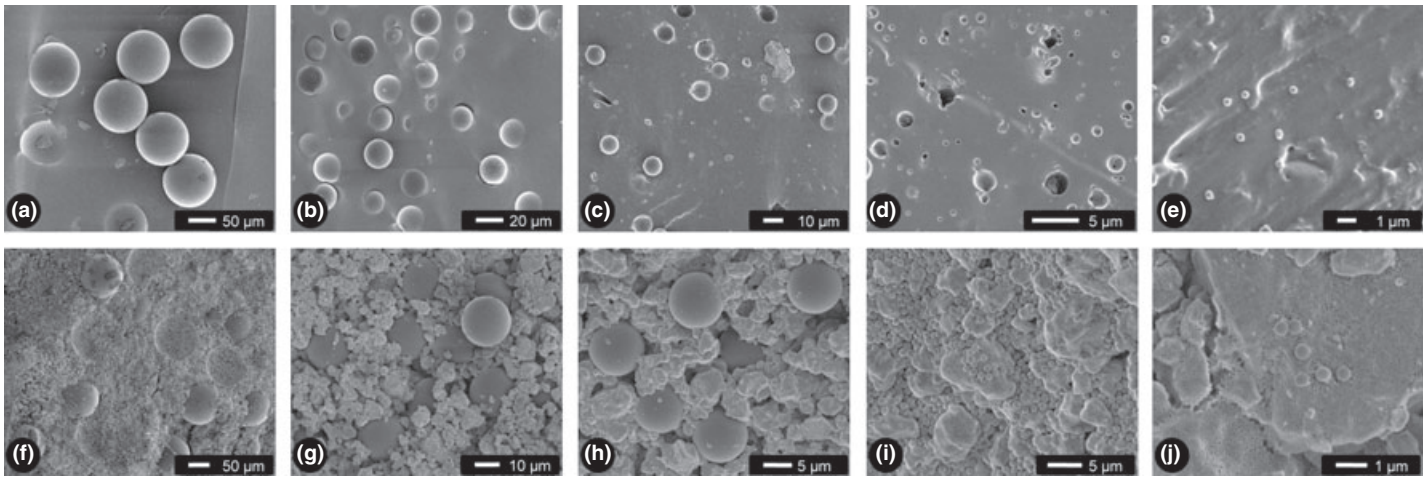

Fig. 1. Scanning electron micrographs of solitaire nano- and microspheres in, respectively, silicone rubber containing (a) 100-µm PS, (b) 20-µm PMA, (c) 10-µm PS, (d) 1-µm SiO_2, and (e) 500-nm SiO_2 spheres, and calcium phosphate matrix containing (f) 100-µm PMA, (g) 20-µm PMA, (h) 10-µm PS, (i) 1-µm SiO_2, and (j) 500-nm SiO_2 spheres.

matrices. When using nano-CT, gray value ranges in the radio absorption histograms were 39–138 (mean 55.43 ± 25.7) for silicone matrices and 50–187 (mean 89.3 ± 25.8) for CPC matrices.

Due to the more uniform radiodensity of the silicone matrix, the microspheres could be easily discriminated in the obtained histogram. The more irregular texture and variation in radiodensity in the CPC allowed for less sensitivity (Fig. 2).

There was no significant difference in the mean gray values of both silicone and CPC samples when using micro- and nano-CT. *P*-values were 0.804 and 0.593 for silicone and CPC, respectively.

Implants

At the end of the 4-week implantation time, one implant was found to be lost. All other implants could be harvested, and there were no visible signs of an excessive inflammatory response or adverse tissue reaction.

Micro- and nano-CT evaluation

Using micro-CT, the total field of view (8.7 mm), containing the implant with a surrounding 500-µm-wide bone area, could be analyzed at 4.37 µm resolution in terms of pixel size. No scattering of the thin Ti layer applied on the PMMA implant surface was found. The PMMA implant and the bone were visible at high magnification (Fig. 3a,b). Morphological details of the bone were restricted to overall structure including the shape of the trabeculae. The extraction of the 3D VOI from the total sample is shown in Fig. 4a,b.

Using nano-CT, even at 2 µm resolution, the limited FOV (2.56 mm) included the entire ROI. Similar to micro-CT, no scattering artifacts were found. Compared with micro-CT, in the nano-CT, a much higher histomorphological details of bone and other tissues could be detected (Fig. 3d,e). Even the structure of the osteons and small blood vessels was clearly visible (Fig. 3g).

For both CT techniques and histology, the BA, BIC, and BV percentage results and obtained paired t-test data are listed in Table 2.

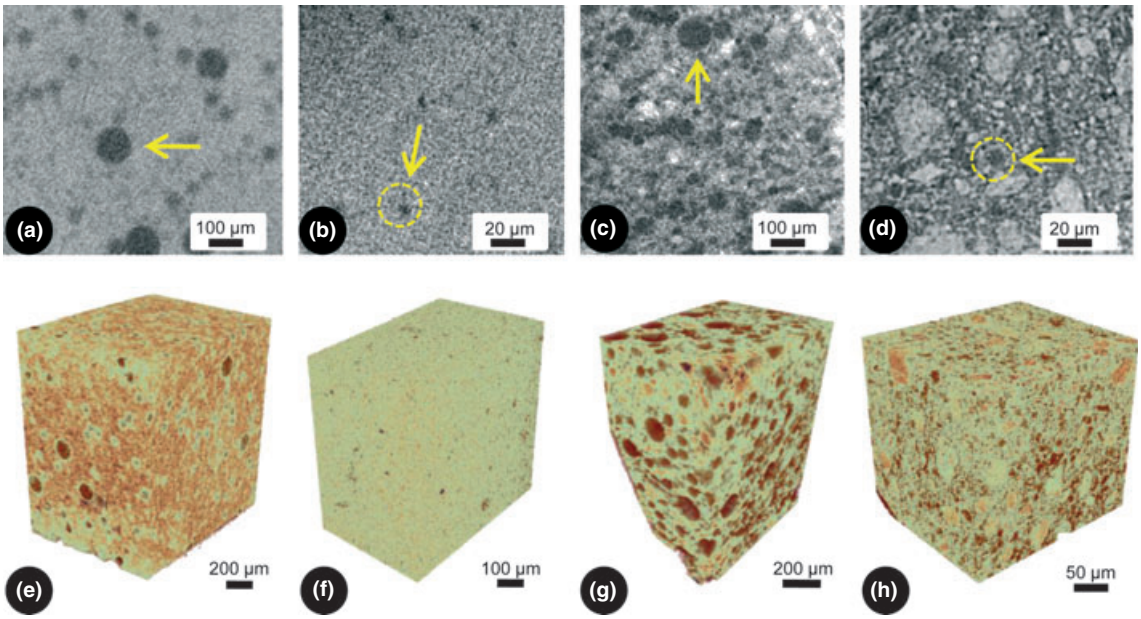

Fig. 2. (a–d) Single 2D micro-CT X-ray images and (e–h) 3D volume reconstruction models of (a, b, e, f) silicone and (c, d, g, h) calcium phosphate cement (CPC) matrices containing, respectively, (a, c, e, g) Ø 100-µm and (b, d, f, h) Ø 10-µm microspheres.

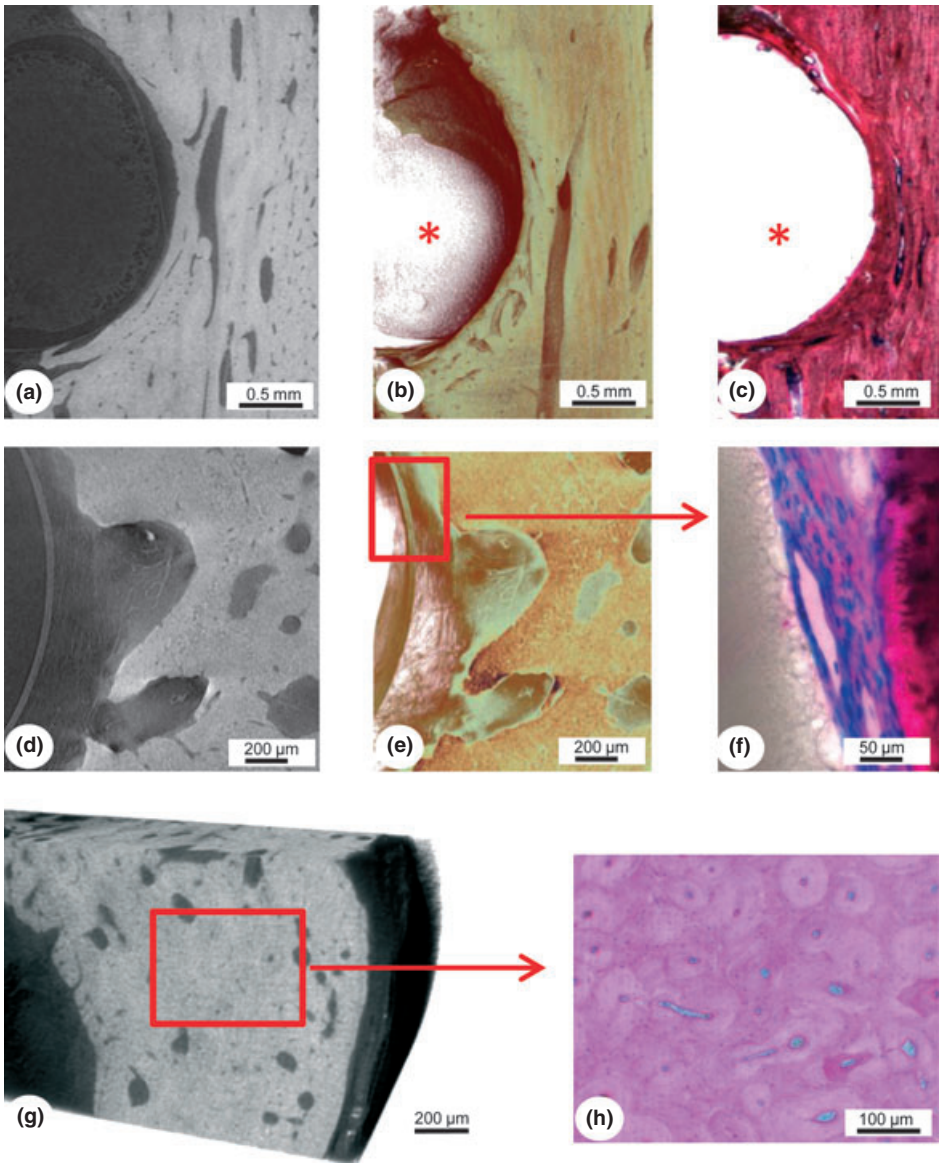

Fig. 3. (a, b) Micro-CT analysis showing implant (*) and bone. (a) single 2D X-ray image at 3 µm resolution, (b) 4-µm^3-voxel-sized 3D volume reconstruction and (c) corresponding histologically stained microscopic slice at 50× magnification. (d, e) Nano-CT analysis showing (d) detailed 2D X-ray image with titanium-coated implant and bone part at 500 nm resolution and (e) corresponding 3D volume reconstruction at 500 nm^3 voxel size. (f) Blue-stained layers of stromal cells lining the pre-existing bone (red–pink) at the bone–implant (gray) surface at 400× magnification. Histological details of osteons in both (g) micro-CT and (h) histology at 100× magnification.

Histological evaluation

Histological sections showed excellent preservation of the bone morphology when embedded in epoxy resin. Because of sample loss and tissue processing, 8 of the 9 samples were finally suitable for final histological analysis. The outline of the Ti-coated PMMA implant was always visible. Pre-existing and newly formed bone was clearly visible. In areas where no bone contact existed, locally a thin layer of stromal cells was lining the implant interface (Fig. 3f). Moreover, histological details as osteons and small blood vessels were clearly visible due to sub-micron resolution (Fig. 3h).

Different bone cell types were clearly visible when using magnifications with pixel sizes up to 0.27 µm. Figure 4c,d visualizes the extraction of the 2D ROI from the histologically stained slice for analysis. Quantification of the BA and BIC of the histological slices is listed in Table 2.

Comparative analysis of CT and histomorphometric data

Statistical comparison of the micro-CT, nano-CT, and histomorphometric paired data showed no significant difference in BA ($P = 0.869$) and BIC ($P = 0.881$) for micro-CT versus histology. In contrast, BA and BIC as assessed in nano-CT were always significantly lower compared with micro-CT ($P = 0.040$ and $P = 0.064$) as well as histology ($P = 0.051$ and $P = 0.052$). BV could not be determined in 2D histomorphometric analysis. For BV, a significantly lower value was found in nano-CT compared with the micro-CT analysis. Notable was also the large diversity in standard deviations for nano-CT (from 35 up to 295%) compared with micro-CT and light microscopy.

Discussion

This study aimed to evaluate spatial resolution and sensitivity of micro- versus nano-CT, including a comparative validation of both techniques versus light microscopical imaging as the gold standard. Overall, it was found that nano-CT provided better resolution, which proved to result in a detail of observation close to histological assessment. However, in terms of quantification, micro-CT showed to result in a more reliable assessment of bone healing parameters matching histomorphometry. Although the image acquisition principles between nano- and micro-CT are similar, there are limitations in sample size. For nano-CT, the achievable volume of interest is smaller, which affects the reliability of the obtained data. In this case, the measurement turned out to be too low. In addition, the individual measurements showed a large statistical scattering resulting in higher diversity of the standard deviations. Therefore, a direct comparison between both CT techniques reveals a more optimal resolution for nano-CT, but a superior capacity for quantification for micro-CT. Thus, both techniques should be regarded as complementary on the basis of details and accuracy.

Considering the current study design, several remarks have to be made. First, the comparative steps were performed using standardized samples made of silicone rubber and ceramic material. This was done purposely, as these two matrices exhibit completely different radio absorption coefficients, hardness, and texture. As a consequence, they provide the optimal means to assess resolution and sensitivity of the used CT systems. Resolution in nano-CT was found to be significantly better, but sensitivity appeared to be similar. Probably, the use of synchrotron micro-CT with a high-intensity monochromatic X-ray beam, combined with phase contrast–enhanced imaging, is a better approach to increase sensitivity (Stiller et al.

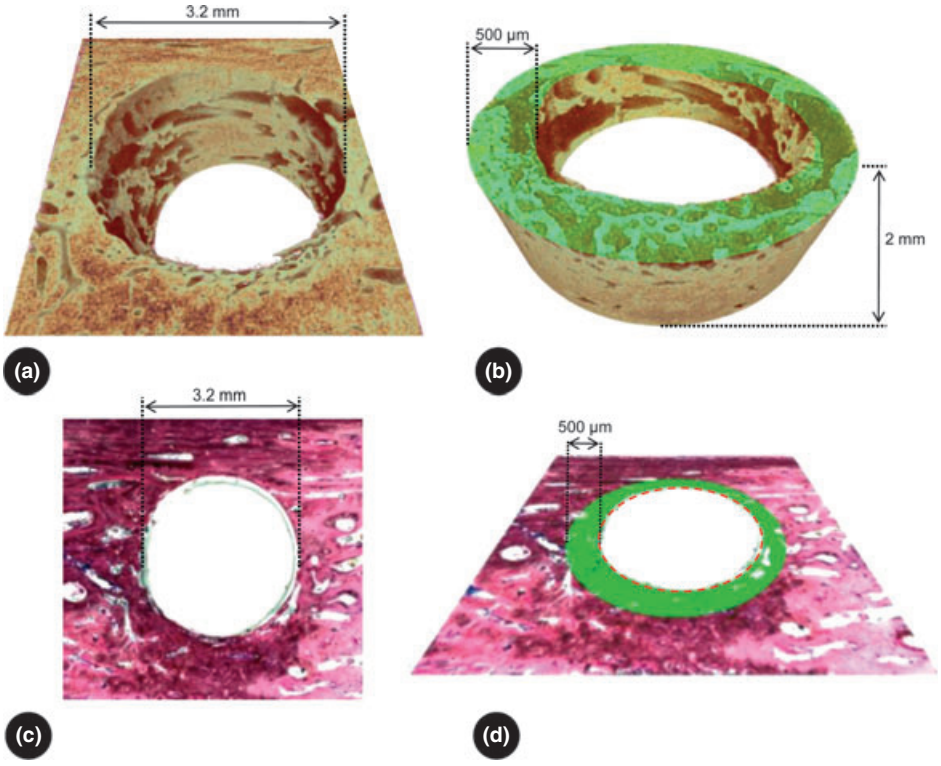

Fig. 4. (a–d) Visualization and selection of bone area (BA) and bone–implant contact (BIC) in micro-CT and histomorphometry analysis. (a) 3D volume reconstruction of bone with transparent implant part, (b) selection of 3D VOI (500 µm width and 2 mm in height) extracted from the bone (BA in green, BIC in red), (c) histologically stained slice part and corresponding (d) BA selection (green) and BIC (red).

Table 2. **Mean and SD of the bone area (BA), bone–implant contact (BIC), and bone volume BV percentage in micro-CT, nano-CT, and histology. Shown are number of measurements (N), compared groups, mean difference (MD), 95% confidence interval (CI), and *P* value for BA, BIC, and BV**

		T-test			
	Mean ± SD	*N*	Compared groups	MD (95% CI)	P value
BA micro-CT	86.3 ± 6.8	3	BA micro-CT vs. BA nano-CT	21.4 (2.3, 40.5)	0.040
BA nano-CT	65.5 ± 11.0	7	BA micro-CT vs. BA histology	0.2 (−3.0, 3.5)	0.869
BA histology	84.1 ± 8.0	3	BA nano-CT vs. BA histology	−18.3 (−39.1,2.6)	0.064
BIC micro-CT	84.0 ± 4.0	3	BIC micro-CT vs. BIC nano-CT	21.5 (−0.1,43.1)	0.051
BIC nano-CT	62.8 ± 11.7	7	BIC micro-CT vs. BIC histology	0.3 (−4.4, 5.0)	0.881
BIC histology	82.5 ± 5.9	3	BIC nano-CT vs. BIC histology	−19.1 (−38,8, 0.5)	0.052
BV micro-CT	81.4 ± 5.5	3	BV micro-CT vs. BV nano-CT	26.7 (−58.4, 111.8)	0.157
BV nano-CT	55.4 ± 7.4				

2009; Yue et al. 2010; Appel et al. 2011) and result in a better sensitivity.

For the comparative evaluation of CT and histological imaging, Ti-coated PMMA implants were placed in the mandibles of Beagle dogs. This implant design was chosen as the most reliable model to quantitate bone healing parameters, as the use of solid titanium implants affects the CT assessment negatively, due to electron-scattering artifacts (Shalabi et al. 2007). Even when specific combined metal filters are used to reduce scattering at the implant surface (Cha et al. 2009). A polymer implant behaves superior due to the diminished occurrence of X-ray scattering, while the surface coating of titanium serves as a close representation of a solid titanium implant. PMMA was chosen as the implant core because Perilli et al. (2007) reported that this polymer is very suitable to study structural parameters of human bone biopsies with micro-CT without obtaining undesirable artifacts.

Besides these aspects related to the CT imaging, a second reason to apply a PMMA-based implant was based on the ease of histological processing. Previously, it was shown that polycarbonate plastic implants, vapor-coated with a layer 120–250 nm of titanium, were applicable for implant research purposes. Such implants were integrated in rabbit bone at 12 weeks of implantation and subsequently could even be processed for electron microscopy (Linder et al. 1983). Albrektsson & Hansson (1985) corroborated such results in a later study, using a 100-nm titanium or zirconium coating, which enabled light and electron microscopy to study the host bone response in high details up to protein attachment level. Thus, our current study followed such principle as well. Because our implant was made of PMMA, for subsequent histological analyses, embedding in epoxy was preferable over routine MMA embedding.

The final validity of CT measurements was performed in comparison with such histological analysis. Of course, no direct comparison could be made as the implant was split in an upper part for CT and lower part for histology. Still, Britz et al. (2010) showed that the matching of the same images, but acquired via different techniques, can also not always be performed at a high accuracy. Histological processing of the samples can result in minor loss of form; moreover, there will always be intrinsic differences in thickness and localization between histological sections in contrast to the CT-reconstructed cross sections. Others compared the use of micro-CT and histology for the evaluation of cortical bone structure and were capable of obtaining a very close correlation between the three-dimensional micro-CT parameters versus two-dimensional histological sections (Particelli et al. 2011). Herein, we assumed that bone morphology was similar between upper (CT) and lower (histology) parts of the implant for regions less than 500 µm apart. The present study confirmed the correlation between micro-CT and histology for the analysis of bone parameters, as also had been determined earlier (Stoppie et al. 2005, 2007). In contrast, the use of nano-CT was found to be less accurate, resulting in lower values compared with micro-CT and light microscopical histomorphometry. The explanation for this observation is that micro-CT is able to study larger samples (~centimeter range) compared with nano-CT (~millimeter range). In addition, when nano-CT is used at nanometer resolution, analysis of only a very limited VOI is possible. This will always result in over- or underestimation errors during quantification. As a second consequence, also the diversity of the standard deviation is large.

Only a very limited number of publications are available describing the use of stand-alone nano-CT systems for the

analysis of bone tissue (Salmon & Sasov 2007; van Hove et al. 2009). Salmon et al. explored the resolution limitations of nano- and micro-CT when studying the ultrastructure of bone. The juvenile murine fibula was chosen as a useful site for nano-CT imaging due to the requirements of a very small specimen size for attaining optimum resolution. A range of histomorphometric parameters were generated including bone area, osteocyte lacuna characteristics, and cellular resorption and formation factors. Nevertheless, no validation of obtained parameters versus other measuring techniques was implemented.

van Hove et al. (2009) studied the osteocyte morphology in human tibiae with a different bone mineral density (BMD) using confocal laser scanning microscopy (CLSM) and nano-CT. The latter technique quantitatively determined 3D morphology and alignment of osteocytes and osteocyte lacunae in human proximal tibial bone with relatively low (osteopenic), medium (osteoarthritic), and high (osteopetrotic) BMD.

Both CLSM and nano-CT demonstrated significant differences in osteocyte 3D morphology in all pathologies. Shape differences in terms of elongation and roundness were found, but there was little difference in cell size. On the other hand, statistical analysis showed a significant difference in the sizes of the osteocyte lacunae. As this study was carried out at cellular level, again limitations to sample size or VOI are less relevant compared with the current work.

In conclusion, this study showed that micro-CT analysis is an efficient tool to quantitate bone healing parameters at the bone–implant interface, especially when using titanium-coated PMMA implants. Nano-CT is not suitable for such quantification, but reveals complementary morphological information rivaling histology.

References

Albrektsson, T. & Hansson, H.-A. (1985) Interface analysis of titanium and zirconium bone implants. *Biomaterials* **6**: 97–101.

Appel, A., Anastasio, M.A. & Brey, E.M. (2011) Potential for imaging engineered tissues with X-ray phase contrast. *Tissue Engineering: Part B Reviews* **17**: 321–330.

Banhart, J. (2008) Advanced Tomographic Methods in Materials Research and Engineering, 1st edition, 145–149, Oxford: Oxford University Press.

Bonnet, N., Laroche, N., Vico, L., Dolleans, E., Courteix, D. & Benhamou, C.L. (2009) Assessment of trabecular bone microarchitecture by two different x-ray microcomputed tomographs: a comparative of the rat distal tibia using Skyscan and Scanco devices. *Medical Physics* **36**: 1286–1297.

Britz, H.M., Jokihaara, J., Leppanen, O.V., Jarvinen, T. & Cooper, D.M. (2010) 3D visualization and quantification of rat cortical bone porosity using a desktop micro-CT system: a case study in the tibia. *Journal of Microscopy* **240**: 32–37.

Calvo Guirado, J.L., Ortiz Ruiz, A.J., Negri, B., López Marí, L., Rodriguez Barba, C. & Schlottig, F. (2009) Histological and histomorphometric evaluation of immediate implant placement on a dog model with a new implant surface treatment. *Clinical Oral Implants Research* **21**: 308–315.

Cha, J.-Y., Lim, J.-K., Song, J.-W., Sato, D., Kenmotsu, M., Inoue, T. & Park, Y.-C. (2009) Influence of the length of the loading period after placement of orthodontic mini-implants on changes in bone histomorphometry: microcomputed tomographic and histologic analysis. *The International Journal of Oral & Maxillofacial Implants* **24**: 842–849.

Chappard, C., Marchadier, A. & Benhamou, C.L. (2008) Side-to-side and within-side variability of 3D bone microarchitecture by conventional micro-computed tomography of paired iliac crest biopsies. *Bone* **43**: 203–208.

van Hove, R.P., Nolte, P.A., Vatsa, A., Semeins, C. M., Salmon, P.L., Smit, T.H. & Klein-Nuland, J. (2009) Osteocyte morphology in human tibiae of different bone pathologies with different bone mineral density – Is there a role for mechanosensing? *Bone* **45**: 321–329.

Junker, R., Manders, P.J.D., Wolke, J., Borisov, Y., Braceras, I. & Jansen, J.A. (2010b) Bone-reaction adjacent to microplasma sprayed CaP-coated oral implants subjected to occlusal load; an experimental study in the dog. Part III: marginal bone and soft tissue healing-long term results. *Clinical Oral Implants Research* **21**: 189–200.

Junker, R., Manders, P.J.D., Wolke, J., Borisov, Y. & Jansen, J.A. (2010a) Bone reaction adjacent to microplasma sprayed CaP-coated oral implants subjected to occlusal load, an experimental study in the dog. Part I: short-term results. *Clinical Oral Implants Research* **21**: 1251–1263.

Junker, R., Manders, P.J.D., Wolke, J., Borisov, Y. & Jansen, J.A. (2011) Bone reaction adjacent to microplasma sprayed calcium phosphate-coated oral implants subjected to occlusal load, an experimental study in the dog. *Clinical Oral Implants Research* **22**: 135–142.

Linder, L., Albrektsson, T., Brånemark, P.-I., Hansson, H.-A., Ivarsson, B., Jönsson, U. & Lundström, I. (1983) Electron microscopic analysis of the bone – titanium interface. *Acta Orthopaedica Scandinavica* **54**: 45–52.

van der Lubbe, H.B., Klein, C.P. & de Groot, K. (1988) A simple method for preparing thin (10 micron) histological sections of undecalcified plastic embedded bone with implants. *Stain Technology* **63**: 171–176.

Particelli, F., Mecozzi, L., Beraudi, A., Montesi, M., Baruffaldi, F. & Viceconti, M. (2011) A comparison between micro-CT and histology for the evaluation of cortical bone: effect of polymethylmethacrylate embedding on structural parameters. *Journal of Microscopy* **245**: 302–310.

Perilli, E., Baruffaldi, F., Visentin, M., Bordini, B., Traina, F., Cappello, A. & Viceconti, M.J. (2007) MicroCT examination of human bone specimens: effects of polymethylmethacrylate embedding on structural parameters. *Journal of Microscopy* **225**: 192–200.

Salmon, P.L. & Sasov, Y.A. (2007) Application of nano-CT and high-resolution micro-CT to study bone quality and ultrastructure, scaffold biomaterials and vascular networks. In: Qin, L., Genant, H.K., Griffith, J. & Leung, K.-S., eds. Advanced Bioimaging Technologies in Assessment of the Quality of Bone and Scaffold Materials. Techniques and Applications. 1st edition, 323–331. Heidelberg: Springer Verlag Berlin.

Sasov, A., Liu, X. & Salmon, P.L. (2008) Compensation of mechanical inaccuracies in micro-CT and nano-CT. In: Stock, S.R., ed. Developments in X-ray Tomography VI, Proc. Of SPIE. Vol. **7078**, 1–9. Bellingham: SPIE.

Schouten, C., Meijer, G.J., van den Beucken, J.J.J.P. & Spauwen, P.H.M. (2009) The quantitative assessment of peri-implant bone responses using histomorphometry and micro-computed tomography. *Biomaterials* **30**: 4539–4549.

Shalabi, M.M., Wolke, J.G.C., Cuijpers, V.M.J.I. & Jansen, J.A. (2007) Evaluation of bone response to titanium-coated polymethyl methacrylate resin (PMMA) implants by X-ray tomography. *Journal of Materials Science. Materials in Medicine* **18**: 2033–2039.

Stiller, M., Rack, A., Zabler, S., Goebbels, J., Dalügge, O., Jonscher, S. & Knabe, S. (2009) Quantification of bone tissue regeneration employing ß-tricalcium phosphate by three-dimensional non-invasive synchrotron micro-tomography – A comparative examination with histomorphometry. *Bone* **44**: 619–628.

Stock, S.R. (2009) Micro-Computed Tomography, Methodology and Applications, 1st edition, 85–92. Baca Raton: CRC Press, Taylor & Francis Group.

Stoppie, N., Waerden van der, J.-P., Jansen, J.A., Duyck, J., Wevers, M. & Naert, I.E. (2005) Validation of microfocus computed tomography in the evaluation of bone implant specimens. *Clinical Implant Dentistry and Related Research* **7**: 87–94.

Stoppie, N., Wevers, N. & Naert, I.E. (2007) Feasibility of detecting trabecular bone around percutaneous titanium implants in rabbits by in vivo microfocus computed tomography. *Journal of Microscopy* **228**: 55–61.

Yue, S., Lee, P.D., Poologasundarampillai, G., Yao, Z., Rockett, P., Devlin, A.H., Mitchell, C. A., Konerding, M.A. & Jones, J.R. (2010) Synchrotron X-ray microtomography for assessment of bone tissue scaffolds. *Journal of Materials Science. Materials in Medicine* **21**: 847–853.

Zou, W., Hunter, N. & Swain, M.V. (2011) Application of polychromatic μCT for mineral density determination. *Journal of Dental Research* **90**: 18–30.